Efficient Chromatic-Number-Based Multiqubit Decoherence and Crosstalk Suppression

Amy F. Brown[1,2,*] and Daniel A. Lidar[1,2,3,4,5]

[1] *Department of Physics and Astronomy, University of Southern California, Los Angeles, California 90089, USA*
[2] *Center for Quantum Information Science & Technology, University of Southern California, Los Angeles, California 90089, USA*
[3] *Ming Hsieh Department of Electrical and Computer Engineering, University of Southern California, Los Angeles, California 90089, USA*
[4] *Department of Chemistry, University of Southern California, Los Angeles, California 90089, USA*
[5] *Quantum Elements, Inc., Thousand Oaks, California, USA*

(Received 4 February 2025; revised 29 April 2025; accepted 22 May 2025; published 18 June 2025)

The performance of quantum computers is hindered by decoherence and crosstalk, which cause errors and limit the ability to perform long computations. Dynamical decoupling is a technique that alleviates these issues by applying carefully timed pulses to individual qubits, effectively suppressing unwanted interactions. However, as quantum devices grow in size, it becomes increasingly important to minimize the time required to implement dynamical decoupling across the entire system. Here, we present "chromatic Hadamard dynamical decoupling" (CHaDD), an approach that efficiently schedules dynamical decoupling pulses for quantum devices with arbitrary qubit connectivity. By leveraging Hadamard matrices, CHaDD achieves a circuit depth that scales linearly with the chromatic number of the connectivity graph for general two-qubit interactions, assuming instantaneous pulses. This includes ZZ crosstalk, which is prevalent in superconducting quantum processing units (QPUs). The scaling of CHaDD represents an exponential improvement over all previous multiqubit decoupling schemes for devices with connectivity graphs the chromatic number of which grows at most polylogarithmically with the number of qubits. For graphs with a constant chromatic number, the scaling of CHaDD is independent of the number of qubits. We report on experiments we have conducted using IBM QPUs that confirm the advantage conferred by CHaDD. Our results suggest that CHaDD can become a useful tool for enhancing the performance and scalability of quantum computers by efficiently suppressing decoherence and crosstalk across large qubit arrays.

DOI: 10.1103/1d4l-73x6

I. INTRODUCTION

Quantum computers contain interconnected qubits that experience decoherence and control errors due to spurious interactions with the environment and surrounding qubits. This adversely affects the ability of such devices to retain or process information for periods of time longer than the decoherence timescale, which is necessary for achieving a quantum advantage over classical computers [1]. In order to surmount this obstacle, considerable attention has been devoted to developing methods that mitigate these deleterious effects, among which dynamical decoupling (DD) has recently been shown to play an important role. DD is an error-suppression technique that averages out undesired Hamiltonian terms by applying deterministic [2–5] or random sequences of scheduled pulses [6,7]. Originally designed to suppress low-frequency noise in nuclear magnetic resonance [8–11], DD effectively decouples the quantum system from both external noise due to decoherence [12–16] and internal noise due to undesired always-on interactions [17–22]. DD has recently found numerous applications in quantum information processing, e.g., in noise characterization [23–29] and improving algorithmic performance [30–35].

Most of the attention in improving performance through DD has focused on the development of DD sequences that achieve high perturbation-theory-order noise cancellation [36–45], robustness to pulse errors [46–49], or reduction of the requirements for quantum error correction [50–54] and error avoidance [55–57]. Much less attention has been paid to developing efficient DD pulse sequences for simultaneously decoupling multiple interconnected qubits and studies of this topic date primarily to early results using

*Contact author: afbrown@usc.edu

Hadamard matrices and orthogonal arrays [17,58–64], along with more recent developments [18,20–22,65,66]. This problem grows in complexity for qubit layouts that are more highly connected, i.e., as the qubit graph degree grows. It is generally recognized that a higher graph degree is desirable [67,68], as this reduces the overhead associated with coupling geometrically distant qubits.

In this paper, we introduce "chromatic Hadamard dynamical decoupling" (CHaDD), which provides an efficient solution to completely decoupling an arbitrary qubit-interaction graph $G=(V,E)$, where V is the vertex (i.e., qubit) set and E is the edge (i.e., qubit-qubit coupling) set. There are two relevant notions of efficiency: (i) the total power consumed by a pulse sequence per decoupling cycle, quantified in terms of the pulse repetition rate (PRR), i.e., the average number of pulses per unit time; and (ii) the circuit depth per cycle, where simultaneous pulses are counted as a single pulse.

Concerning circuit depth, until recently, efficient schemes were thought to be at most linear in the total number of qubits $n=|V|$ [61–63] for instantaneous ("bang-bang" [2]) pulses. Then, it was established that the scaling of complete decoupling of a ZZ crosstalk graph [69] could be stated in terms of the chromatic number of the graph $\chi(G)$ (an idea dating back to Refs. [17,18]), i.e., the minimum number of distinct colors required to properly color the graph, instead of the number of qubits, albeit with exponential scaling, $2^{\chi(G)}$ [22].

Here, we show that it is possible to achieve *efficient* universal first-order decoupling. Namely, we prove that in general, the circuit depth scales linearly with the chromatic number, with an improved prefactor for single-axis decoupling (e.g., the special case of ZZ crosstalk). This is an exponential improvement over the single-axis crosstalk-suppression result of Ref. [22], as well as over all previous multiaxis decoupling schemes building on Hadamard matrices or orthogonal arrays [58–63] for graphs with a chromatic number that scales at most polylogarithmically in n. The schemes of Refs. [61–63] achieve parity with CHaDD when $\chi(G)\sim n$, as is the case with trapped-ion or neutral-atom devices with all-to-all connectivity [67,70]. In devices with a constant chromatic number, such as all current superconducting quantum computing hardware, the scaling of CHaDD is independent of n, providing a significant advantage over decoupling schemes that scale linearly with the number of qubits. In such cases, CHaDD can further help diagnose and suppress crosstalk between non-natively coupled qubits corresponding to an effective connectivity graph with a higher chromatic number.

Going beyond the efficient circuit-depth scaling of CHaDD, we also consider the PRR (i.e., power consumption) metric at fixed chromatic number. We demonstrate both theoretically and experimentally that CHaDD achieves similar or better performance at a lower PRR than standard "achromatic" DD pulse sequences, i.e., sequences that are blind to the chromatic number of the underlying qubit-connectivity graph. Namely, we show that CHaDD reduces the PRR by 20–33%, depending on the specific CHaDD variant.

The structure of this paper is as follows. In Sec. II, we provide pertinent background on graph coloring, the error model, and dynamical decoupling. In Sec. III, we define CHaDD and several variants designed to suppress multiaxis decoherence and to improve robustness against pulse errors. We prove our main theorems concerning the circuit-depth efficiency of CHaDD and discuss several illustrative examples. In Sec. IV, we provide experimental tests of CHaDD and its variants using IBM superconducting quantum processing units (QPUs) and demonstrate that, as predicted by our theory, CHaDD exhibits a better PRR than previously known sequences. We conclude in Sec. V and discuss various possible generalizations and open problems suggested by our work. The appendices provide additional technical details in support of the main text, as well as additional confirmation of our experimental results obtained on different IBM QPUs.

II. BACKGROUND

A. Graph coloring

Coloring is the assignment of colors (labels) to the vertices of a graph such that no two adjacent vertices share the same color. The chromatic number is related to the graph degree: Brooks' theorem states that for a connected graph G with maximum degree Δ, $\chi(G)\leq\Delta$ except when G is a complete graph or an odd cycle, in which case $\chi(G)=\Delta+1$ [71,72]. Moreover, if the maximum degree of the subgraph induced on a vertex $v\in V$ and its neighborhood is $\Delta(v)$, then $\chi(G)\geq\Delta(v)+1$, which provides a lower bound using the neighborhood degree [73]. Lower bounds also exist in terms of the adjacency matrix [74,75]. Finding the chromatic number is one of Karp's 21 NP-complete problems [76] but in many cases of interest, we do not need to exactly know $\chi(G)$: since Δ is often a constant in the quantum computing context, we may in such cases simply replace $\chi(G)$ by the graph degree Δ to obtain an upper bound.

B. Error model

Consider a system of qubits occupying the vertices V of a graph G. We are concerned with the suppression of undesired interactions between this system and its environment and the suppression of undesired internal system terms arising, e.g., due to crosstalk. Letting $\{\sigma_v^\alpha\}_{\alpha\in\{x,y,z\}}$ denote the Pauli matrices acting only on qubit v, quite generally this scenario can be represented in terms of the following Hamiltonian:

$$H=H_1+H_2, \tag{1a}$$

$$H_1 = \sum_{\alpha\in\{x,y,z\}} H_1^\alpha\ ,\ \ H_2 = \sum_{\alpha,\beta\in\{x,y,z\}} H_2^{\alpha\beta}, \tag{1b}$$

$$H_1^\alpha = \sum_{v\in V} \sigma_v^\alpha \otimes B_v^\alpha\ ,\ \ H_2^{\alpha\beta} = \sum_{\{(u,v)\in E\ \mid\ u<v\}} \sigma_u^\alpha \sigma_v^\beta \otimes B_{uv}^{\alpha\beta}. \tag{1c}$$

In Eq. (1c), we sum over ordered pairs of vertices and $B_v^\alpha = \omega_v^\alpha \tilde{B}_v^\alpha$ ($B_{uv}^{\alpha\beta} = J_{uv}^{\alpha\beta}\tilde{B}_{uv}^{\alpha\beta}$), where $\tilde{B}_v^\alpha$ ($\tilde{B}_{uv}^{\alpha\beta}$) are dimensionless operators that act purely on the environment, and ω_v^α ($J_{uv}^{\alpha\beta}$) are the corresponding couplings with dimensions of energy. The unperturbed evolution given by the "free-evolution unitary" $f_\tau = \exp(-i\tau H)$ is then generally nonunitary and decoherent. In the case of undesired internal terms, the $\tilde{B}_v^\alpha$ ($\tilde{B}_{uv}^{\alpha\beta}$) represent the identity operator on all qubits but v (and u). f_τ is then unitary but subject to coherent error, including both control errors and crosstalk.

C. Dynamical decoupling

DD is based on the application of short and narrow ("bang-bang" [2]) pulses $P_{\alpha,v}(\theta) = \exp[-i(\theta/2)\sigma_v^\alpha]$. Here, we are concerned primarily with the case of π pulses and denote $X_v = P_{x,v}(\pi) = -i\sigma_v^x$ (an "X pulse") and similarly for Y and Z. It is well known that to suppress decoherence and undesirable terms in the system Hamiltonian (such as crosstalk or unintended single-qubit terms), it suffices to apply π pulses at regular intervals, as long as these pulses cycle over the elements of a group [4]. Applying such a sequence synchronously to all qubits would suppress H_1 but not H_2, since it would commute with the pulses. To dynamically decouple several qubits in a manner that suppresses both H_1 and H_2, one can use Hadamard matrices and orthogonal arrays to schedule the pulses in such a way that prevents the pulses from commuting with H_2 [58–63]. However, such schemes are suboptimal if they do not account for the qubit-connectivity graph; recent work that does has resulted in a scheme requiring a cost of $2^{\chi(G)}$ pulses to decouple all ZZ crosstalk in a graph G [22] (the special case $H = H_2^{zz}$). We now show how this can be both exponentially reduced in cost and extended to deal with a general Hamiltonian H [Eq. (1)].

III. RESULTS

A. Single-axis CHaDD

We first specialize to the case in which H_1 and H_2 do not include pure-x-type terms. This includes ZZ crosstalk.

Theorem 1 (single-axis CHaDD). Assume that the free-evolution unitary is $f_\tau = e^{-i\tau H}$, where H is given by Eq. (1). Then, a circuit depth of $\chi \le N \le 2\chi$, involving only X pulses, suffices to cancel to first order in τ all terms in H excluding H_1^x and H_2^{xx} on a qubit-connectivity graph G with chromatic number χ.

Proof. Let χ be the chromatic number of the graph G corresponding to the Hamiltonian H given by Eq. (1) and let $\phi : V \to \{1, 2, \ldots, \chi(G)\} \equiv C$ be a proper χ-coloring of the graph G. Define $V_c \equiv \{v \in V \mid \phi(v) = c\}$, i.e., the set of all vertices of the same color c, and $E_{c_1,c_2} \equiv \{(u, v) \in E \mid u < v, \phi(u) = c_1, \phi(v) = c_2\}$, i.e., the set of all ordered pairs of vertices of colors c_1 and c_2, respectively, joined by edges in E. Now we return to Eq. (1c) and group the terms according to the coloring of G:

$$H_1^\alpha = \sum_{c\in C}\sum_{v\in V_c} \sigma_v^\alpha\ ,\quad H_2^{\alpha\beta} = \sum_{c_1\neq c_2}\ \sum_{(u,v)\in E_{c_1,c_2}} \sigma_u^\alpha\sigma_v^\beta. \tag{2}$$

We have suppressed the bath operators in Eq. (2) for notational simplicity; they will not matter in our calculations below, since we only consider first-order time-dependent perturbation theory through the Baker-Campbell-Hausdorff (BCH) expansion; the effect of noncommuting bath operators appears only to second order.

If we conjugate the free-evolution unitary f_τ by X pulses applied to all qubits of the same color c, i.e., by $\widetilde{X}_c \equiv \bigotimes_{v\in V_c} X_v$, we flip the sign of all σ_v^y and σ_v^z terms corresponding to qubits v of color c, since they anticommute with $\widetilde{X}_c$. Similarly, for the two-body terms, we flip the sign of all $\sigma_u^\alpha\sigma_v^\beta$ terms where one of the qubits u and v is of color c and the corresponding Pauli operator anticommutes with X. Thus,

$$\widetilde{X}_c f_\tau \widetilde{X}_c^\dagger = \exp\left[-i\tau\left(\widetilde{H}_{1,c} + \widetilde{H}_{2,c}\right)\right], \tag{3a}$$

$$\widetilde{H}_{1,c} = \sum_{\alpha\in\{x,y,z\}} \widetilde{H}_{1,c}^\alpha\ ,\quad \widetilde{H}_{2,c} = \sum_{\alpha,\beta\in\{x,y,z\}} \widetilde{H}_{2,c}^{\alpha\beta}, \tag{3b}$$

$$\widetilde{H}_{1,c}^\alpha = \widetilde{X}_c H_1^\alpha \widetilde{X}_c^\dagger = \sum_{c'\in C} (-1)^{\delta_{cc'}(1-\delta_{\alpha x})} \sum_{v\in V_{c'}} \sigma_v^\alpha, \tag{3c}$$

$$\widetilde{H}_{2,c}^{\alpha\beta} = \widetilde{X}_c H_2^{\alpha\beta} \widetilde{X}_c^\dagger = \sum_{c_1\neq c_2} (-1)^{\delta_{cc_1}(1-\delta_{\alpha x})}(-1)^{\delta_{cc_2}(1-\delta_{\beta x})} \sum_{(u,v)\in E_{c_1,c_2}} \sigma_u^\alpha\sigma_v^\beta. \tag{3d}$$

Note that $\widetilde{H}_{1,c}^x = H_1^x$ and $\widetilde{H}_{2,c}^{xx} = H_2^{xx}$. To go beyond qubits of a single color c, we form a criterion for determining whether to conjugate f_τ by $\widetilde{X}_c$ for a given color c at time step j according to the Hadamard matrix.

Let $\nu = \lfloor \log_2 \chi \rfloor + 1$, $N = 2^\nu$, and consider the $N \times N$ Hadamard matrix

$$W_\nu \equiv W_1^{\otimes\nu} = \frac{1}{\sqrt{N}} \sum_{i,j\in\{0,1\}^\nu} (-1)^{i\cdot j} |i\rangle\langle j|, \tag{4}$$

where W_1 is the standard 2×2 Hadamard matrix and where the dot product is the bit-wise scalar product with addition modulo 2. Below, we use i and j to denote an integer or its binary expansion (i.e., $i = i_0 i_i \dots i_{\nu-1}$), depending on the context.

Consider any injective function $g : C \to \{1, 2, \dots, N-1\}$ that maps distinct colors in C to distinct rows $i > 0$ of the Hadamard matrix W_ν. Note that ν is the number of bits needed to account for every color $c \in C$. For every such color, we use row $i = g(c)$ to schedule the decoupling scheme for the qubits in V_c: at each time step $j = 0, 1, \dots, N-1$, if $\langle i | W_\nu | j \rangle = (-1)^{i \cdot j} = -1$ (the core property of the Hadamard matrix that we need), i.e., if $i \cdot j \equiv 1 \mod 2$, we conjugate f_τ by $\widetilde{X}_c$. Equivalently, for each color c at each time step j, we conjugate f_τ by $\widetilde{X}_c^{g(c)\cdot j}$. The resulting unitary-control propagator across all colors $c \in C$ at time step j is then

$$U_j^x \equiv \overline{X}_j f_\tau \overline{X}_j^\dagger, \quad \overline{X}_j \equiv \bigotimes_{c \in C} \widetilde{X}_c^{g(c)\cdot j}. \tag{5}$$

The only difference from Eq. (3) is that now the indicator functions are generalized from a single color (such as $\delta_{cc'}$) to the set of all colors dictated by the Hadamard matrix at time step j, i.e., to $g(c) \cdot j$. Consequently, Eq. (3) is replaced by

$$U_j^x = \exp\left[-i\tau \left(\overline{H}_{1,j} + \overline{H}_{2,j}\right)\right], \tag{6a}$$

$$\overline{H}_{1,j} = \sum_{\alpha \in \{x,y,z\}} \overline{H}_{1,j}^{\alpha}, \quad \overline{H}_{2,j} = \sum_{\alpha,\beta \in \{x,y,z\}} \overline{H}_{2,j}^{\alpha\beta}, \tag{6b}$$

$$\overline{H}_{1,j}^{\alpha} = \overline{X}_j H_1^\alpha \overline{X}_j^\dagger = \sum_{c \in C} (-1)^{g(c)\cdot j(1-\delta_{\alpha x})} \sum_{v \in V_c} \sigma_v^\alpha, \tag{6c}$$

$$\overline{H}_{2,j}^{\alpha\beta} = \overline{X}_j H_2^{\alpha\beta} \overline{X}_j^\dagger = \sum_{c_1 \neq c_2} (-1)^{g(c_1)\cdot j(1-\delta_{\alpha x})} (-1)^{g(c_2)\cdot j(1-\delta_{\beta x})} \sum_{(u,v) \in E_{c_1,c_2}} \sigma_u^\alpha \sigma_v^\beta. \tag{6d}$$

Similarly, $\overline{H}_{1,j}^x = H_1^x$ and $\overline{H}_{2,j}^{xx} = H_2^{xx}$, meaning that pure-$x$ terms are invariant.

Each U_j^x takes one time step of length τ. Then, using the BCH expansion, the entire sequence of N time steps and total duration $T = N\tau$ has the following unitary:

$$\prod_{j=0}^{N-1} U_j^x = \exp\left[-i\tau \sum_{j=0}^{N-1} \overline{H}_{1,j} + \overline{H}_{2,j}\right] + \mathcal{O}\left(T^2\right). \tag{7}$$

Now, observe that the single-qubit sum $\sum_j \overline{H}_{1,j} = N H_1^x$, since $\sum_{j=0}^{N-1} (-1)^{g(c)\cdot j} = 0 \,\forall\, g(c) \neq 0$, where we have used the fact that all rows $i = g(c) > 0$ of the Hadamard matrix have entries that add up to zero. Similarly, the two-qubit sum $\sum_j \overline{H}_{2,j} = N H_2^{xx}$, since $\sum_{j=0}^{N-1} (-1)^{g(c_1)\cdot j} (-1)^{g(c_2)\cdot j} = \delta_{g(c_1),g(c_2)} = 0$, where we have used the fact that the Hadamard matrix W_ν is orthogonal, i.e., $\delta_{i_1,i_2} = \langle i_1 | W_\nu^T W_\nu | i_2 \rangle = \frac{1}{N} \sum_{j \in \{0,1\}^\nu} (-1)^{i_1 \cdot j} (-1)^{i_2 \cdot j}$, and that g is injective, i.e., $c_1 \neq c_2 \implies i_1 = g(c_1) \neq g(c_2) = i_2$. Thus,

$$U^x \equiv \prod_{j=0}^{N-1} U_j^x = \exp\left[-iT(H_1^x + H_2^{xx})\right] + \mathcal{O}\left(T^2\right) \tag{8}$$

and we have eliminated to first order in τ all nonpure-x terms in H_1 and H_2. The total number of time steps, i.e., the circuit depth, is $N = 2^\nu = 2^{\lfloor \log_2 \chi \rfloor + 1}$, i.e., $\chi \le N \le 2\chi$. ■

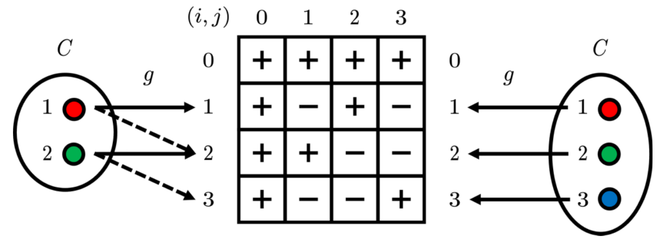

FIG. 1. Color-to-row maps for 2-colorable (left) and 3-colorable (right) graphs. The solid arrows correspond to an unbalanced schedule and the dashed arrows to a balanced schedule. Middle: the Hadamard matrix W_2.

The sequence that explicitly provides the circuit alluded to in the statement of Theorem 1, and which is constructed in the proof of this theorem, is as follows.

Definition 1 (single-axis x-type CHaDD). The sequence $U^x = \prod_{j=0}^{N-1} U_j^x$ with U_j^x given in Eq. (5) is called single-axis x-type CHaDD. Other single-axis CHaDD sequences are obtained by replacing x with another axis.

We illustrate single-axis x-type CHaDD for a few examples with low chromatic numbers.

Since $\chi(G) \ge 2$ for graphs with $|E| \ge 1$, for single-axis CHaDD we use graphs G with $\chi(G) = 2, 3$, i.e., $\nu = \lfloor \log_2 \chi(G) \rfloor + 1 = 2$. By Theorem 1, a circuit depth of $N = 2^\nu = 4$ is then sufficient to cancel all nonpure-x interactions (e.g., ZZ crosstalk) and qubit decoherence to first order, scheduled according to the Hadamard matrix W_2 shown in Fig. 1 (middle).

Per Theorem 1, the first row ($i = 0$) is not used. For $\chi(G) = 3$, we must use all three of the remaining rows $i = 1, 2, 3$, but for $\chi(G) = 2$, we can choose any pair of rows.

1. Example 1: Single-axis CHaDD for $\chi(G) = 2$

Consider a square grid of qubits with nearest-neighbor coupling, as in Fig. 2 (top and middle). This graph G is 2-colorable (bipartite), i.e., there exists a proper 2-coloring $\phi : V \to \{1, 2\} \equiv C$. Examples of such graphs include the

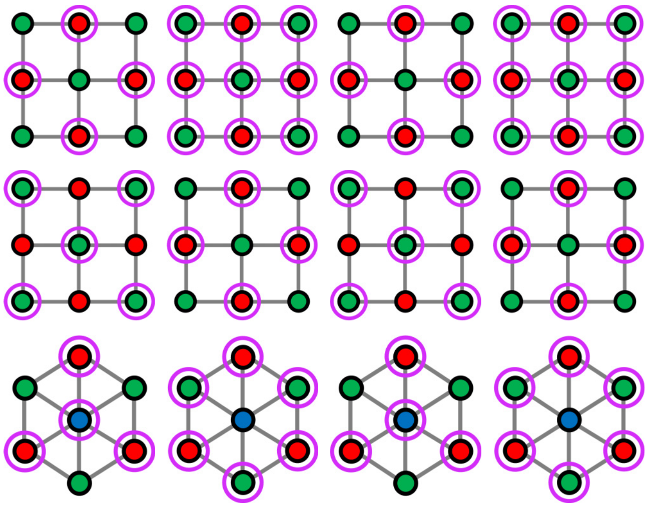

FIG. 2. Examples of schedules for 2-colorable (top and middle) and 3-colorable (bottom) graphs. The purple circles indicate DD pulses and time flows from left to right. Top row: an unbalanced schedule for a 2-colorable graph [Eq. (9)]. Middle row: a balanced schedule for a 2-colorable graph [Eq. (10)]. Bottom row: an unbalanced schedule for a 3-colorable graph [Eq. (11)].

Rigetti Ankaa family of chips [77] and the IBM heavy-hex layout [78].

Let us choose the identity color-to-row map $i = g(c) = c$ so that colors $c = 1, 2$ correspond to rows $i = 1, 2$, respectively, as in Fig. 1 (left, solid arrows). We conjugate the free evolution f_τ by all $\widetilde{X}_i$ operators for which $\langle i| W_2 |j\rangle = -1$ for each time step (column) j. This readily yields $U_0^x = f_\tau$ for the first interval, $U_1^x = \widetilde{X}_1 f_\tau \widetilde{X}_1^\dagger$ for the second, $U_2^x = \widetilde{X}_2 f_\tau \widetilde{X}_2^\dagger$ for the third, and, since $\overline{X}_3 = \widetilde{X}_1\widetilde{X}_2$, finally $U_3^x = (\widetilde{X}_1\widetilde{X}_2) f_\tau (\widetilde{X}_1\widetilde{X}_2)^\dagger$ for the last interval. Taking the product of all unitaries yields the *unbalanced* schedule

$$U^x = \prod_{j=0}^{3} U_j^x = \widetilde{X}_1\widetilde{X}_2 f_\tau \widetilde{X}_1 f_\tau \widetilde{X}_1\widetilde{X}_2 f_\tau \widetilde{X}_1 f_\tau, \tag{9}$$

wherein a pulse is applied to all 1-colored qubits every τ but only every 2τ to the 2-colored qubits (see Fig. 2, top).

A *balanced* schedule results if, instead, we choose $i = g(c) = c + 1$, as in Fig. 1 (left, dashed arrows), resulting in $U_0^x = f_\tau$, $U_1^x = \widetilde{X}_2 f_\tau \widetilde{X}_2^\dagger$, $U_2^x = (\widetilde{X}_1\widetilde{X}_2) f_\tau (\widetilde{X}_1\widetilde{X}_2)^\dagger$, and $U_3^x = \widetilde{X}_1 f_\tau \widetilde{X}_1^\dagger$, so that

$$U^x = \prod_{j=0}^{3} U_j^x = \widetilde{X}_1 f_\tau \widetilde{X}_2 f_\tau \widetilde{X}_1 f_\tau \widetilde{X}_2 f_\tau, \tag{10}$$

wherein a pulse is applied alternately to 1- and 2-colored qubits every 2τ. This schedule is illustrated in Fig. 2 (middle) and may be considered preferable due to its symmetry and lower overall pulse count of four single-color pulses versus six for the unbalanced schedule. It is an interesting question to identify the general conditions for a balanced schedule directly from the Hadamard matrix in arbitrary dimensions.

2. Example 2: Single-axis CHaDD for $\chi(G) = 3$

An example for which $\chi(G) = 3$ is a triangular grid (Fig. 2, bottom). We must now use all three rows $i = 1, 2, 3$ of the Hadamard matrix W_2, and g can only be a permutation. Consider the identity $i = g(c) = c$, as in Fig. 1 (right). We obtain $U_0^x = f_\tau$, $\overline{X}_1 = \widetilde{X}_1\widetilde{X}_3$ so that $U_1^x = (\widetilde{X}_1\widetilde{X}_3) f_\tau (\widetilde{X}_1\widetilde{X}_3)^\dagger$ and, similarly, $U_2^x = (\widetilde{X}_2\widetilde{X}_3) f_\tau (\widetilde{X}_2\widetilde{X}_3)^\dagger$ and $U_3^x = (\widetilde{X}_1\widetilde{X}_2) f_\tau (\widetilde{X}_1\widetilde{X}_2)^\dagger$. Thus,

$$U^x = \prod_{j=0}^{3} U_j^x = \widetilde{X}_1\widetilde{X}_2 f_\tau \widetilde{X}_1\widetilde{X}_3 f_\tau \widetilde{X}_1\widetilde{X}_2 f_\tau \widetilde{X}_1\widetilde{X}_3 f_\tau, \tag{11}$$

an unbalanced schedule using eight single-color pulses (see Fig. 2, bottom). This is the single-axis CHaDD sequence, simply referred to as "CHaDD," implemented in our experiments below.

B. Multiaxis CHaDD

As is the case in the single-qubit XY4 sequence [11], we can obtain *multiaxis* CHaDD sequences by concatenating single-axis CHaDD sequences about perpendicular axes [36]. This leads to a concatenated multiaxis CHaDD protocol requiring a quadratic circuit depth in $\chi(G)$ (see Appendix A). However, as we show next, for $\chi(G) \geq 3$, a more efficient multiaxis CHaDD protocol is possible that retains the linear scaling in $\chi(G)$. For $\chi(G) = 2$, both protocols require a circuit depth of 16.

Rather than associating a color with a single row of a Hadamard matrix, we need three rows per color for multiaxis CHaDD. To explain the protocol, we need to first introduce some additional terminology [58–63]. A sign matrix $S_{\chi,N}$ is a $\chi \times N$ matrix with ± 1 entries (W_χ is a special case). The Schur product $C = A \circ B$ of two $\chi \times N$ sign matrices A and B is the entry-wise product $C_{ij} = A_{ij}B_{ij}$. A set of $\chi \times N$ sign matrices is Schur-closed if it is closed under the Schur product. A *Schur subset* is a set of rows of sign matrices that multiply entry-wise to $+ + \cdots +$. Note that Schur subsets are Schur-closed. We will identify Schur subsets with colors.

Theorem 2 (multiaxis CHaDD). Under the same assumptions as in Theorem 1, a circuit depth of $3\chi + 1 \leq N \leq 2(3\chi + 5)$, involving only single-qubit Pauli pulses, suffices to cancel to first order in τ *all* terms in H on a qubit-connectivity graph G with chromatic number χ.

The proof combines ideas from Refs. [58,62] with our single-axis CHaDD approach.

Proof. Assign to each color c a Schur subset via an injective function h. For a given Schur subset $h(c)$, label its three rows $h(c;x)$, $h(c;y)$, and $h(c;z)$. Define the $\chi \times N$ sign matrix S_α, where $\alpha \in \{x,y,z\}$, as the matrix whose rows are $\{h(c;\alpha)\}_{c\in C}$. These sign matrices S_α are Schur-closed. This implies that for each fixed (c,j)'th entry, $([S_x]_{cj}, [S_y]_{cj}, [S_z]_{cj})$ can only be one of $(+,+,+)$, $(+,-,-)$, $(-,+,-)$, or $(-,-,+)$. These tuples correspond to whether or not a given Pauli operator $\widetilde{\sigma}_{(c,j)}$ acting on all qubits of color c commutes $(+)$ or anticommutes $(-)$ with $(\sigma_v^x, \sigma_v^y, \sigma_v^z)$, where $\phi(v) = c$, i.e., $\widetilde{\sigma}_{(c,j)} = \widetilde{I}_c, \widetilde{X}_c, \widetilde{Y}_c$, and $\widetilde{Z}_c$, respectively.

Then, the unitary-control propagator is $\overline{\sigma}_j \equiv \bigotimes_{c\in C} \widetilde{\sigma}_{(c,j)}$ in time step j and when we conjugate f_τ by $\overline{\sigma}_j$, i.e., $U_j \equiv \overline{\sigma}_j f_\tau \overline{\sigma}_j^\dagger$, the sign acquired by σ_v^α is $[S_\alpha]_{cj}$ if $\phi(v) = c$, while the sign acquired by $\sigma_u^\alpha \sigma_v^\beta$ $(u < v)$ is $[S_\alpha]_{c_1 j} [S_\beta]_{c_2 j}$ if $\phi(u) = c_1$ and $\phi(v) = c_2$:

$$U_j = \exp\left[-i\tau \left(\overline{H}_{1,j} + \overline{H}_{2,j}\right)\right], \tag{12a}$$

$$\overline{H}_{1,j} = \sum_{\alpha\in\{x,y,z\}} \overline{H}_{1,j}^\alpha , \quad \overline{H}_{2,j} = \sum_{\alpha,\beta\in\{x,y,z\}} \overline{H}_{2,j}^{\alpha\beta}, \tag{12b}$$

$$\overline{H}_{1,j}^\alpha = \overline{\sigma}_j H_1^\alpha \overline{\sigma}_j^\dagger = \sum_{c\in C} [S_\alpha]_{cj} \sum_{v\in V_c} \sigma_v^\alpha, \tag{12c}$$

$$\overline{H}_{2,j}^{\alpha\beta} = \overline{\sigma}_j H_2^{\alpha\beta} \overline{\sigma}_j^\dagger = \sum_{c_1\neq c_2} [S_\alpha]_{c_1 j} [S_\beta]_{c_2 j} \sum_{(u,v)\in E_{c_1,c_2}} \sigma_u^\alpha \sigma_v^\beta. \tag{12d}$$

The overall unitary for all N time steps is now

$$U \equiv \prod_{j=0}^{N-1} U_j = \exp\left[-i\tau \sum_{j=0}^{N-1} \overline{H}_{1,j} + \overline{H}_{2,j}\right] + \mathcal{O}\left(T^2\right). \tag{13}$$

To remove all one- and two-local terms, i.e., $\sum_j \overline{H}_{1,j} = 0$ and $\sum_j \overline{H}_{2,j} = 0$, we need $\sum_j [S_\alpha]_{cj} = 0$ and $\sum_j [S_\alpha]_{c_1 j} [S_\beta]_{c_2 j} = 0$. The first condition follows immediately from the fact that these are rows of a Hadamard matrix and the second follows from the fact that each Schur subset has been drawn from different partitions ($c_1 \neq c_2$) of the same Hadamard matrix, so the rows of the sign matrices S_α are orthogonal.

The Hadamard matrix W_ν can be partitioned into exactly $S_e = (2^\nu - 1)/3$ Schur subsets if ν is even and at most $S_o = (2^\nu - 5)/3$ if ν is odd [58] (see also Ref. [79, Theorem 4.1] and Appendix B). Let $\nu = 2k$ and $k \in \mathbb{Z}^+$, so $S_e(k) = (2^{2k} - 1)/3$ and $S_o = (2^{2k+1} - 5)/3$. Since the circuit depth is $N = 2^\nu$, we would like to minimize k. We need at least as many Schur subsets as colors; hence $\min\{S_e(k), S_o(k)\} \geq \chi$. Minimizing k, we have $k = \min\{f_e(\chi), f_o(\chi)\}$, where $f_e(\chi) = \lceil \frac{1}{2}\log_2(3\chi + 1)\rceil$ and $f_o(\chi) = \lceil \frac{1}{2}[\log_2(3\chi + 5) - 1]\rceil$. Thus, we obtain $N = \min\{2^{2\lceil \frac{1}{2}\log_2(3\chi+1)\rceil}, 2^{2\lceil \frac{1}{2}[\log_2(3\chi+5)-1]\rceil+1}\} \in \Theta(\chi)$, i.e., $3\chi + 1 \leq N \leq 2(3\chi + 5)$. ■

We explain the upper and lower bounds in Appendix C. Since N is a step function in χ, these bounds are loose (e.g., $N = 16$ for $2 \leq \chi \leq 5$, and $N = 32$ for $6 \leq \chi \leq 9$) but they are nearly tight envelopes.

The sequence that explicitly provides the circuit alluded to in the statement of Theorem 2, and which is constructed in the proof of this theorem, is as follows.

Definition 2 (multiaxis CHaDD). The sequence $U = \prod_{j=0}^{N-1} U_j$ with $U_j \equiv \overline{\sigma}_j f_\tau \overline{\sigma}_j^\dagger$, $\overline{\sigma}_j \equiv \bigotimes_{c\in C} \widetilde{\sigma}_{(c,j)}$ is called multiaxis CHaDD.

We give an explicit example of multiaxis CHaDD below.

1. Example 3: Multiaxis CHaDD for $\chi = 3$

For $2 \leq \chi \leq 5$, $N = 16$, so $\nu = 4$ is even, and W_4 can be partitioned into $(2^\nu - 1)/3 = 5$ Schur subsets [58]. Sign matrices S_x, S_y, and S_z for $\chi \leq 5$ are [60, Ex. 2]:

$$S_x = \begin{pmatrix} + & + & + & + & + & + & + & + & - & - & - & - & - & - & - & - \\ + & + & - & - & - & - & + & + & + & + & - & - & - & - & + & + \\ + & - & - & + & + & - & - & + & - & + & + & - & - & + & + & - \\ + & - & - & + & - & + & + & - & - & + & + & - & + & - & - & + \\ + & + & - & - & + & + & - & - & - & - & + & + & - & - & + & + \end{pmatrix}, \tag{14a}$$

$$S_y = \begin{pmatrix} + & + & + & + & - & - & - & - & + & + & + & + & - & - & - & - \\ + & - & + & - & - & + & - & + & + & - & + & - & - & + & - & + \\ + & + & - & - & + & + & - & - & + & + & - & - & + & + & - & - \\ + & + & - & - & - & - & + & + & - & - & + & + & + & + & - & - \\ + & - & + & - & - & + & - & + & - & + & - & + & + & - & + & - \end{pmatrix}, \tag{14b}$$

$$S_z = \begin{pmatrix} + & + & + & + & - & - & - & - & - & - & - & - & + & + & + & + \\ + & - & - & + & + & - & - & + & + & - & - & + & + & - & - & + \\ + & - & + & - & + & - & + & - & - & + & - & + & - & + & - & + \\ + & - & + & - & + & - & + & - & + & - & + & - & + & - & + & - \\ + & - & - & + & - & + & + & - & + & - & - & + & - & + & + & - \end{pmatrix}. \tag{14c}$$

These matrices are closed under the Schur product and the set consisting of the ith row of each of three sign matrices S_α forms a Schur subset. We need at least as many Schur subsets as colors, so we can use the above matrices to schedule up to five colors.

For $\chi = 3$, let us assign color c to the Schur subset consisting of row $i = h(c) = c$ from each of the three sign matrices above. The $\chi \times N$ sign matrices S_α for this example are then the middle three rows of the sign matrices provided above. We must look at the entries corresponding to color c and time step j in each of the three sign matrices, i.e., $([S_x]_{cj}, [S_y]_{cj}, [S_z]_{cj})$ to determine which Pauli operation conjugates f_τ. All colors in time step $j = 0$ have entries $(+,+,+)$ corresponding to Pauli operator $\tilde{\sigma}_{(c,0)} = \tilde{I}_c$, so we have $\overline{\sigma}_0 = I$ and $U_0 = f_\tau$. In time step $j = 1$, color $c = 1$ has tuple $([S_x]_{1,1}, [S_y]_{1,1}, [S_z]_{1,1}) = (+,-,-)$ corresponding to $\tilde{\sigma}_{(1,1)} = \tilde{X}_1$, color $c = 2$ has tuple $([S_x]_{2,1}, [S_y]_{2,1}, [S_z]_{2,1}) = (-,+,-)$ corresponding to $\tilde{\sigma}_{(2,1)} = \tilde{Y}_2$, and color $c = 3$ has tuple $([S_x]_{3,1}, [S_y]_{3,1}, [S_z]_{3,1}) = (-,+,-)$ corresponding to $\tilde{\sigma}_{(3,1)} = \tilde{Y}_3$, so $\overline{\sigma}_1 = \tilde{X}_1\tilde{Y}_2\tilde{Y}_3$, and $U_1 = \left(\tilde{X}_1\tilde{Y}_2\tilde{Y}_3\right) f_\tau \left(\tilde{X}_1\tilde{Y}_2\tilde{Y}_3\right)^\dagger$. In time step $j = 2$, color $c = 1$ has tuple $(-,+,-)$ corresponding to $\tilde{\sigma}_{(1,2)} = \tilde{Y}_1$, color $c = 2$ has tuple $(-,-,+)$ corresponding to $\tilde{\sigma}_{(2,2)} = \tilde{Z}_2$, and color $c = 3$ has tuple $(-,-,+)$ corresponding to $\tilde{\sigma}_{(3,2)} = \tilde{Z}_3$, so $\overline{\sigma}_2 = \tilde{Y}_1\tilde{Z}_2\tilde{Z}_3$, and $U_2 = \left(\tilde{Y}_1\tilde{Z}_2\tilde{Z}_3\right) f_\tau \left(\tilde{Y}_1\tilde{Z}_2\tilde{Z}_3\right)^\dagger$. Taking the product of all $N = 16$ time steps yields the multiaxis CHaDD sequence:

$$\begin{aligned} U &= \prod_{j=0}^{15} U_j \\ &= \tilde{I}_1\tilde{Z}_2\tilde{X}_3 f_\tau \tilde{X}_1\tilde{Y}_2\tilde{Y}_3 f_\tau \tilde{Z}_1\tilde{X}_2\tilde{X}_3 f_\tau \tilde{X}_1\tilde{Y}_2\tilde{Y}_3 f_\tau \\ &\quad \tilde{I}_1\tilde{X}_2\tilde{Y}_3 f_\tau \tilde{X}_1\tilde{Y}_2\tilde{Y}_3 f_\tau \tilde{Z}_1\tilde{X}_2\tilde{X}_3 f_\tau \tilde{X}_1\tilde{Y}_2\tilde{Y}_3 f_\tau \\ &\quad \tilde{I}_1\tilde{Z}_2\tilde{X}_3 f_\tau \tilde{X}_1\tilde{Y}_2\tilde{Y}_3 f_\tau \tilde{Z}_1\tilde{X}_2\tilde{X}_3 f_\tau \tilde{X}_1\tilde{Y}_2\tilde{Y}_3 f_\tau \\ &\quad \tilde{I}_1\tilde{X}_2\tilde{Y}_3 f_\tau \tilde{X}_1\tilde{Y}_2\tilde{Y}_3 f_\tau \tilde{Z}_1\tilde{X}_2\tilde{X}_3 f_\tau \tilde{X}_1\tilde{Y}_2\tilde{Y}_3 f_\tau. \end{aligned} \tag{15}$$

This is the multiaxis CHaDD sequence implemented in our experiments below.

C. A robust CHaDD variant

DD sequences with robustness to pulse imperfections are known [47,48]. The "universally robust" (URn) family of sequences, for even $n \geq 4$, consists of n π pulses about various axes in the x-y plane [48]. The simplest sequence, UR4, consists of the uniform interval sequence $X\bar{X}\bar{X}X$, where $X = P_x(\pi)$ and $\bar{X} = P_x(-\pi)$. Analogously, we define a robust version of the single-axis x-type CHaDD sequence by replacing X with $\bar{X}$ where necessary to match the UR4 sequence pattern.

For example, the $\chi = 3$ CHaDD sequence given in Eq. (11) consists of colors 1, 2, and 3 receiving $XXXX$, $IXIX$, and $XIXI$, respectively. We need a minimum of four pulses on each color to form a robust sequence, so we replace these with $X\bar{X}\bar{X}XX\bar{X}\bar{X}X$, $IXI\bar{X}I\bar{X}IX$, and $XI\bar{X}I\bar{X}IXI$, which doubles the circuit depth compared to CHaDD. We denote this robust CHaDD variant "CHaDD-R4," or CHaDD-R for brevity. Note that CHaDD-R promotes the underlying achromatic UR4 sequence to an efficient multiqubit sequence in the same sense that CHaDD and multiaxis CHaDD, respectively, promote the XX and XY4 sequences.

D. Pulse repetition rate at fixed chromatic number

Theorems 1 and 2 characterize CHaDD in terms of the scaling of circuit depth with chromatic number. However, with an eye toward an experimental comparison between the CHaDD variants and their underlying achromatic sequences at *fixed* chromatic number, it is also meaningful to quantify performance in terms of pulse repetition rate (PRR), i.e., the average number of pulses per unit time. A lower PRR is advantageous, as it means reduced power consumption and, hence, less heat being injected into the system from microwave sources. A lower PRR also implies a reduction in control-error accumulation. The PRR for $\chi = 3$ is illustrated for a few key sequences in Fig. 3. Since the achromatic sequences (XX, XY4, UR4, etc.) do not distinguish qubits by color, they target all qubits in every time step, while CHaDD variants selectively target qubits by color. The result is a PRR that is $1/3$ lower for CHaDD and CHaDD-R than it is for XX and UR4, respectively. Clearly, a sequence achieving equal performance at lower PRR is preferred. We next describe experiments designed to test the performance of CHaDD variants relative to achromatic sequences according to this criterion.

IV. EXPERIMENTS

We have performed experiments on the IBM_BRISBANE 127-qubit QPU. IBM's "heavy-hex" qubit-connectivity

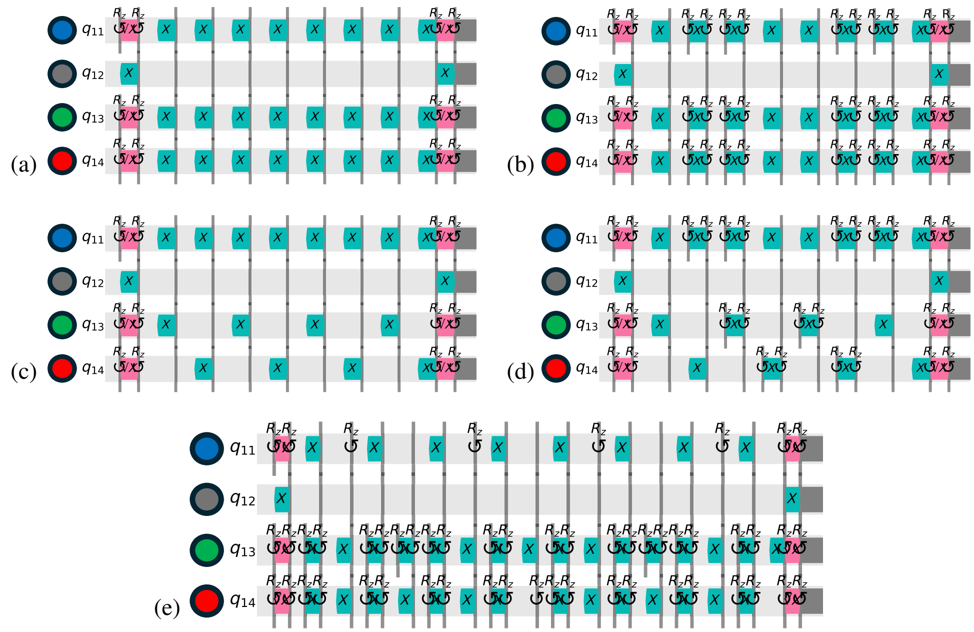

FIG. 3. A four-qubit portion of the 127-qubit $\chi = 3$ experiment time line of (a) XX, (b) UR4, (c) CHaDD, (d) CHaDD-R, and (e) multiaxis CHaDD with red, green, blue (RGB), and gray qubits prepared in the $|+\rangle$ and $|1\rangle$ states, respectively. XX, UR4, and CHaDD are length-4 sequences repeated twice, CHaDD-R is a length-8 sequence repeated once, and multiaxis CHaDD is a length-16 sequence repeated once. The CHaDD sequences (c) and (d) are scheduled according to the color-to-row function $g(1) = 2$, $g(2) = 3$, and $g(3) = 1$, different from that in the bottom row of Fig. 2, and use two pulses per time slot compared to three for their achromatic counterparts (a) and (b), i.e., use 1/3 fewer pulses, resulting in a PRR that is 2/3 that of XX and UR4. During (e) multiaxis CHaDD, the RGB qubits see an average of 38/3 pulses over 16 time steps, resulting in a PRR that is $38/48 \approx 0.79$ that of XY4. To avoid interference effects arising from placing pulses too close together, we set $\tau = 2\delta$ (where δ is the pulse width), and to ensure a correct implementation of $\bar{X}$, we use a symmetric decomposition ($\bar{X} = R_z(-\pi)XR_z(\pi)$, where $R_z(\varphi) \equiv \exp(-i\varphi\sigma^z/2)$ is a virtual-Z gate [80]) for UR4 and CHaDD-R [81].

graphs are 2-colorable, as they lack an odd cycle. Previous work on crosstalk cancellation [20–22] has not presented explicit schemes for $\chi > 2$ and, instead, has focused on 2-colorable graphs (including Rigetti QPUs). To demonstrate the ability of CHaDD to go beyond $\chi = 2$, we embed within the 2-colorable heavy-hex lattice a 3-colorable system graph. This is illustrated in Fig. 4, with "system" qubits colored red, green, and blue (RGB). The remaining "bath" qubits are colored gray.

What distinguishes the system from the bath qubits is that our goal is to suppress both decoherence and crosstalk on the former but not the latter. With this in mind, we recall from the proof of Theorem 1 that the first row of the Hadamard matrix ($i = 0$) is not used to schedule any pulses. Thus, we assign the gray qubits to this row and the red, green, and blue qubits to rows 2, 3, and 1 of W_2, respectively. In this manner, decoherence of the gray qubits is not suppressed, though their crosstalk still is (since row 0 is orthogonal to all the other rows). In addition, while the gray qubits are measured, we discard the corresponding measurement outcomes.

In order to compare different DD sequences, we initialize all qubits in $|0\rangle$, prepare the gray qubits in each of $|0\rangle$, $|+\rangle$, and $|1\rangle$, and prepare the RGB qubits in each of the six Pauli eigenstates, for a total of 18 different preparation-state settings. We perform DD on the RGB qubits, undo the state preparation, and obtain the fidelity of the RGB qubits as the fraction of $|0\rangle$ states that we obtain when measuring all RGB qubits in the σ^z basis over 5000 trials, or "shots." XX, XY4, UR4, and CHaDD are length-4 sequences, CHaDD-R is a length-8 sequence and multiaxis CHaDD is a length-16 sequence. Accordingly, we repeat XX, XY4, UR4, and CHaDD in multiples of 4 up to 80 times, CHaDD-R in multiples of 2 up to 40 times, and multiaxis CHaDD up to 20 times so that each sequence results in 21 data points that take the same amount of time to collect. We report the average over the 18 preparation-state settings.

In Fig. 5, we collect the results from three achromatic DD sequences and three CHaDD variants, along with free evolution (idle). XY4, UR4, multiaxis CHaDD, and CHaDD-R are the top-performing sequences. Note that these sequences have much smaller 1σ error bars than the others, indicating less susceptibility to variation in initial state conditions and a better ability to preserve arbitrary initial states. We compare the top sequences in Fig. 6, where XY4, UR4, and CHaDD-R are seen to be roughly tied for top performance.

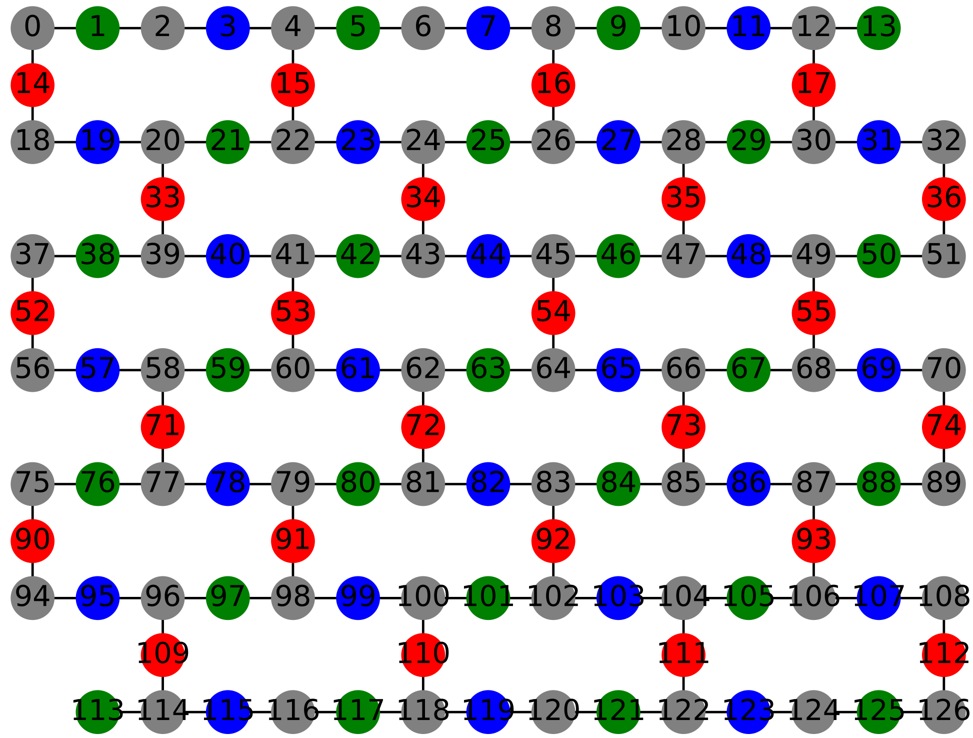

FIG. 4. The embedded 3-coloring of the 127 qubit heavy-hex graph consisting of system qubits (red, green, blue) and bath qubits (gray).

CHaDD, multiaxis CHaDD, and CHaDD-R can be thought of as the CHaDD variants of the underlying achromatic XX, XY4, and UR4 sequences, respectively. In this sense, the CHaDD variants either outperform or are on par with their underlying achromatic sequences, most notably CHaDD versus XX in Fig. 5. Crucially, the CHaDD variants achieve this performance with a significantly reduced pulse count (or PRR), as also shown in Fig. 6. As noted

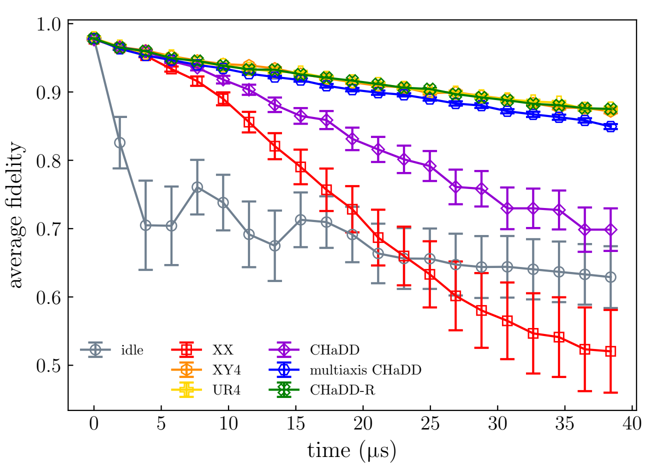

FIG. 5. A comparison of the average initial state preservation fidelity of RGB qubits, averaged over 18 preparation-state settings, for all achromatic DD sequences and their CHaDD counterparts run on IBM_BRISBANE. The error bars here and in all other plots are 1σ.

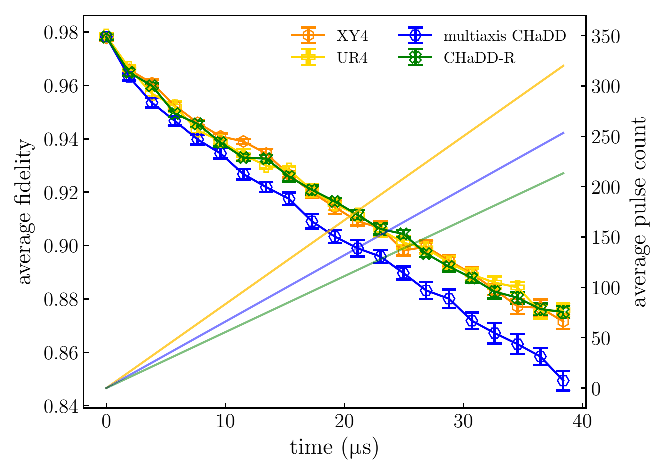

FIG. 6. The average state-preservation fidelity for RGB qubits (left) and the pulse count per RGB qubit (right) of the most-performant DD sequences on IBM_BRISBANE. Multiaxis CHaDD and CHaDD-R are the CHaDD versions of XY4 and UR4, respectively, and they exhibit similar performance, but CHaDD-R has $1/3$ fewer pulses than UR4 and XY4, while multiaxis CHaDD has $1/5$ fewer pulses than XY4 and UR4 (see Fig. 3). Note that the yellow and orange lines overlap, since XY4 and UR4 have the same PRR.

above, CHaDD-R has a 1/3 smaller PRR than UR4. As anticipated, this constitutes a much sparser and hence more power-efficient sequence for the same performance. As mentioned above, a lower PRR also reduces control-error accumulation, which is the likely explanation for the large performance gap between CHaDD and XX, given the latter's absence of inherent robustness against such errors (in contrast, XY4 and UR4 are both robust sequences [48]). At the same time, CHaDD lacks a control-error-suppression mechanism, which explains why it underperforms the robust sequences. This also applies to multiaxis CHaDD, which slightly underperforms CHaDD-R.

While all the chromatic and achromatic sequences decouple all the heavy-hex RGB-gray couplings, only the chromatic sequences additionally suppress the red-green, red-blue, and green-blue next-nearest-neighbor couplings; they do this with a lower PRR than the achromatic sequences, as illustrated in Fig. 3. The fact that the achromatic sequences also decouple the RGB qubits is a peculiarity of the embedding; crosstalk on a native 3-colorable graph would not be decoupled by synchronous achromatic sequences, whereas with the embedding the gray qubits mediate the crosstalk between the RGB qubits, and an achromatic sequence that is applied only to the RGB qubits, as we do here, does suppress crosstalk as a result. To see this, consider, e.g., the interaction $\sigma_R^z\sigma_{\text{gray}}^z + \sigma_{\text{gray}}^z\sigma_B^z$, which anticommutes with, and hence is suppressed by, the XX-sequence pulse $(X_R \otimes I_{\text{gray}})(I_{\text{gray}} \otimes X_B)$ applied only the red (R) and blue (B) qubits. Thus, the embedding creates an artificially favorable setup for the achromatic sequences. To demonstrate this, we have repeated our experiments while letting the latter also target the gray qubits. Consequently, this is a standard 2-coloring of the heavy-hex graph, which has been extensively studied before [20–22]. The result is shown in Fig. 7 and it confirms that the performance of the achromatic sequences is significantly reduced, with strong crosstalk oscillations clearly visible.

Appendix D provides additional experimental results obtained using other IBM QPUs that are in complete qualitative agreement with the conclusions reported in this section.

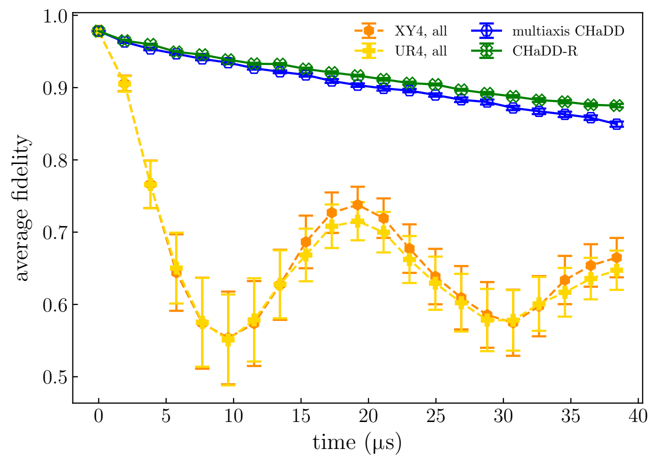

FIG. 7. As in Fig. 5 but with the achromatic sequences XY4 and UR4 applied to all qubits. The multiaxis CHaDD and CHaDD-R data are the same as in Fig. 5. Both CHaDD variants significantly outperform their underlying achromatic sequences in this setting.

V. CONCLUSIONS AND OUTLOOK

We have proposed CHaDD along with both its multiaxis and robust variants. These are first-order DD schemes that are efficient in the chromatic number χ of the qubit connectivity graph, which, as a function of χ, lead to a scaling advantage in the circuit depth required to decouple arbitrary connectivity graphs relative to previously known multiqubit decoupling methods [20–22,58–63,65]. This includes, as a special case, multiqubit ZZ crosstalk decoupling. At fixed χ, we have demonstrated a significant reduction in the pulse repetition rate—and hence, power consumption—required to achieve a performance that is on par with or better than standard achromatic DD sequences.

To generalize CHaDD beyond first-order decoupling is straightforward. For example, concatenation of multiaxis CHaDD with itself is the direct multiqubit generalization of concatenating XY4 with itself, which leads to the single-qubit concatenated DD (CDD) family [36], yielding an extra suppression order in time-dependent perturbation theory with every additional level of concatenation [37,51].

However, concatenation incurs an exponential cost in circuit depth and it would be desirable to be able to replace the uniform pulse intervals used in the construction of single-axis CHaDD with the nonuniform intervals used in the single-qubit Uhrig DD (UDD) sequence family [38], in order to guarantee the same higher-order performance as UDD [40] in the single-axis multiqubit setting. This would directly extend to multiaxis single-qubit decoupling via the quadratic DD (QDD) sequence [43], which requires at most $(m+1)^2$ pulses for order-m suppression in terms of the Dyson-series expansion [44]. Successfully combining CHaDD with QDD would generally be much more efficient than the multiqubit nested UDD (NUDD) sequence, which scales exponentially with the number of qubits [42]. Whether these extensions of CHaDD are possible is an interesting open problem.

It should be possible to generalize CHaDD beyond qubits to multilevel systems by replacing the Pauli matrices used in the proof of Theorem 1 with elements of the generalized Pauli (or Heisenberg-Weyl) group [61,82,83]. CHaDD-R, our robust version of CHaDD, is based on the UR4 sequence; a proper generalization of URn [48] to CHaDD-Rn is an interesting topic for future research.

Finally, it is another interesting open problem to generalize CHaDD from two-local and instantaneous pulses to k-local interactions and bounded controls for n qubits, for which the current state of the art is $\mathcal{O}[n^{k-1}\log(n)]$ [63].

ACKNOWLEDGMENTS

This material is based upon work supported by, or in part by, the U.S. Army Research Laboratory and the U.S. Army Research Office under Contract/Grant No. W911NF2310255. This research was supported by the Office of the Director of National Intelligence (ODNI), the Intelligence Advanced Research Projects Activity (IARPA) and the ARO, under the Entangled Logical Qubits program through Cooperative Agreement No. W911NF-23-2-0216. We gratefully acknowledge Victor Kasatkin and Jenia Mozgunov for helpful discussions.

DATA AVAILABILITY

The data and the notebooks required to recreate the plots in this paper are openly available [84].

APPENDIX A: MULTIAXIS CHaDD VIA CONCATENATION

Corollary A1 (Concatenated multiaxis CHaDD). Assume that the free-evolution unitary is $f_\tau = e^{-i\tau H}$, where H is given by Eq. (1). Then, a circuit depth of $4^{\lfloor \log_2 \chi(G)\rfloor+1} \le 4\chi^2(G)$ is sufficient to completely cancel H to first order in τ on a qubit-connectivity graph G with chromatic number $\chi(G)$.

Proof. It follows immediately from Theorem 1 (by swapping the x and z indices) that a single-axis z-type CHaDD sequence has an overall unitary of

$$U^z \equiv \prod_{j=0}^{N-1} U_j^z = \exp\left[-iT(H_1^z + H_2^{zz})\right] + \mathcal{O}\left(T^2\right). \quad \text{(A1)}$$

If we concatenate the single-axis x- and z-type sequences at every time step, i.e., replace f_τ in $U_j^x = \overline{X}_j f_\tau \overline{X}_j^\dagger$ with the single-axis z-type CHaDD sequence U^z, we obtain $U_j^{xz} \equiv \overline{X}_j U^z \overline{X}_j^\dagger$, so that

$$U^{xz} \equiv \prod_{j=0}^{N-1} U_j^{xz} = \prod_{j=0}^{N-1} \overline{X}_j e^{-iT(H_1^z+H_2^{zz})}\overline{X}_j^\dagger + \mathcal{O}\left(NT^2\right). \quad \text{(A2)}$$

This is just the single-axis x-type CHaDD sequence U^x given by Eq. (8) applied to an effective Hamiltonian $H = H_1^z + H_2^{zz}$ without any H_1^x or H_2^{xx} terms, so it follows from Theorem 1 that this Hamiltonian is completely canceled to first order, i.e.,

$$\prod_{j=0}^{N-1} \overline{X}_j e^{-iT(H_1^z+H_2^{zz})}\overline{X}_j^\dagger = I + \mathcal{O}\left(NT^2\right). \quad \text{(A3)}$$

Hence, the total CHaDD unitary is $U^{xz} = I + \mathcal{O}\left(NT^2\right)$. This requires a circuit depth of $N^2 = 2^{2(\lfloor \log_2 \chi(G)\rfloor+1)} \le 4\chi^2(G)$. ■

Definition A1. The sequence $U^{xz} = \prod_{j=0}^{N-1} U_j^{xz}$ is called concatenated multiaxis CHaDD.

Clearly, replacing x and z with other combinations of orthogonal axes is equivalent to U^{xz}. Thus, U^{xz} can be interpreted as the efficient multiaxis multiqubit generalization of the XY4 sequence [11].

APPENDIX B: CONNECTIONS TO PROJECTIVE GEOMETRY

The properties of Schur subsets of a sign matrix presented by Leung [58] were discovered in a more general form several decades earlier in the projective-geometry community, using the terminology of partial t-spreads in the Desargesian projective space $PG(d,q)$, where d is the dimension and q is the order (number of elements) of the finite field $\mathbb{F}_q$ [79]. In such a space, points and lines are defined in terms of vector spaces over $\mathbb{F}_q$, and the incidence structure obeys the axioms of projective geometry. Desargues' theorem guarantees that any configuration of points and lines that forms a perspective triangle has collinear points, ensuring a well-defined projective structure. A perspective triangle is a configuration in which two triangles are in perspective from a point or a line.

For our purposes, $PG(d,q) = \mathbb{Z}_2^\nu \setminus \{0\}$, $d = \nu - 1$, $q = 2$, $t = 1$, and the size of the partial t-spread is the number of Schur subsets.

In this context, Ref. [79, Thm. 4.1] states that there are no more than $(2^\nu - 5)/3$ Schur subsets for a Hadamard

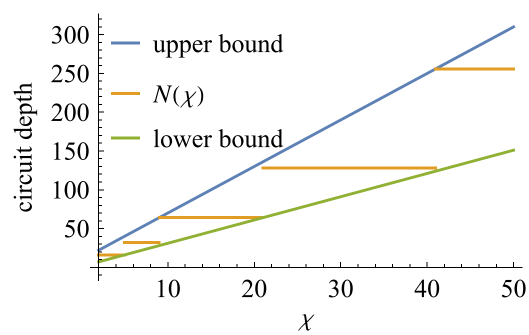

FIG. 8. The circuit depth $N(\chi)$ of multiaxis CHaDD [Eq. (C1)] along with the upper and lower bounds, $2(3\chi + 5)$ and $3\chi + 1$, respectively.

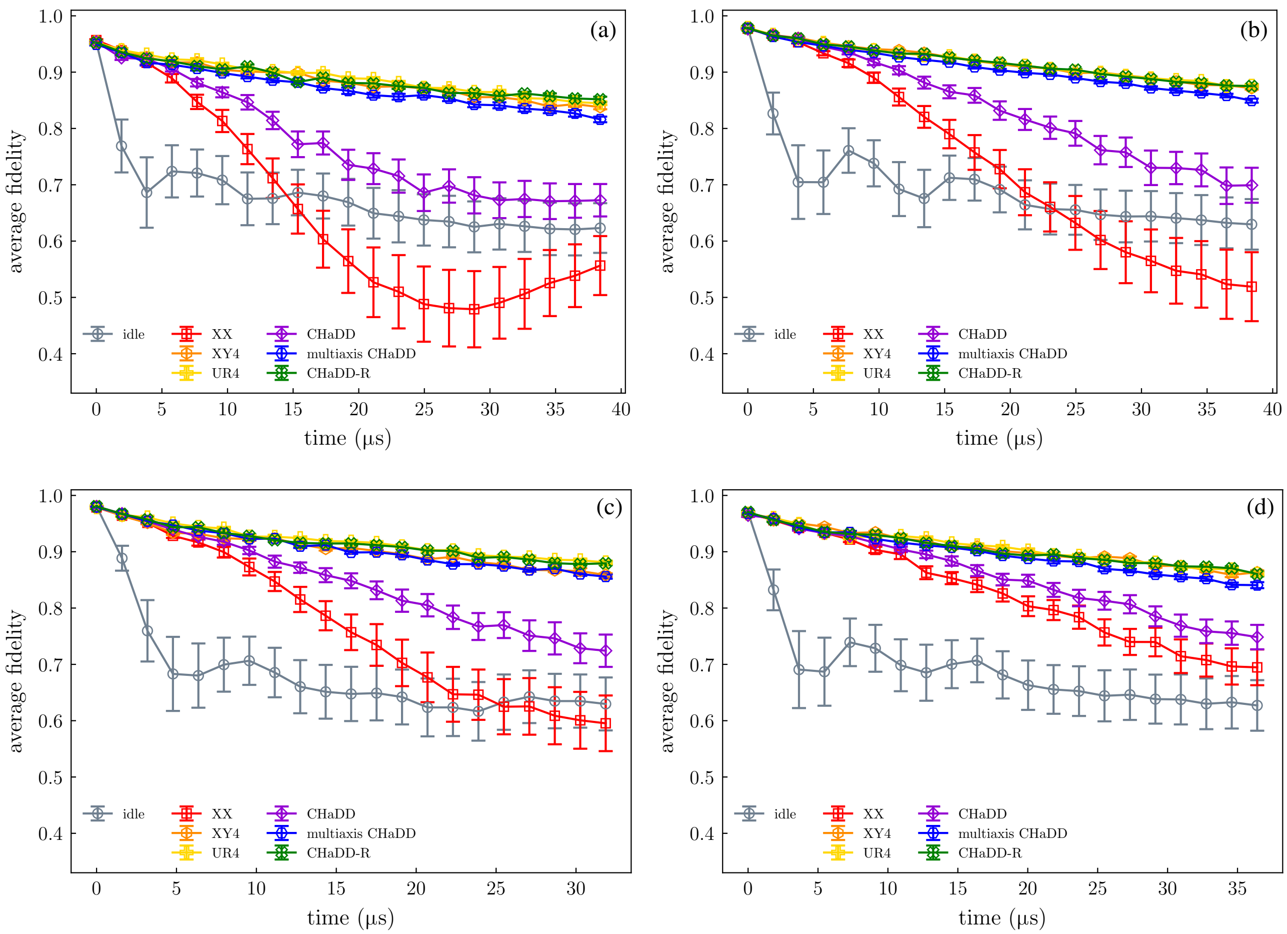

FIG. 9. Comparison across four IBM QPUs. The time axes are different since the duration of single-qubit gates varies: (a) IBM_STRASBOURG, 60 ns; (b) IBM_BRISBANE, 60 ns; (c) IBM_KYIV, 49.78 ns; (d) IBM_SHERBROOKE, 56.89 ns. Different QPUs exhibit different quantitative behaviors, with IBM_STRASBOURG displaying the overall lowest fidelities and largest crosstalk, evidenced by the oscillation in the XX-sequence results.

matrix W_ν with odd ν. For even ν one can pick all $2^\nu - 1$ nontrivial rows of the Hadamard matrix (one row is the trivial row of all $+$), resulting in $(2^\nu - 1)/3$ Schur subsets, so the upper bound is not needed.

Moreover, the bounds for both odd and even ν are achievable: for even ν, Ref. [79] states that this was known before (Results 2.1 and 2.2), and for odd ν this is shown in Theorem 4.2.

APPENDIX C: CIRCUIT DEPTH OF MULTIAXIS CHaDD

In the main text, we have shown that

$$N = \min\{2^{2\lceil \frac{1}{2}\log_2(3\chi+1)\rceil}, 2^{2\lceil \frac{1}{2}[\log_2(3\chi+5)-1]\rceil+1}\} \qquad \text{(C1)}$$

for the circuit depth of multiaxis CHaDD. Here, we derive the upper and lower bounds. It follows from the definitions of S_e and S_o that $2^\nu \geq 3\chi + 1$ and $2^\nu \geq 3\chi + 5$ in the case that ν is even and odd, respectively. Thus, in either case, we have that $N = 2^\nu \geq 3\chi + 1$, establishing a lower bound on the circuit depth regardless of the value of ν. Now consider that we wish to choose the smallest value of ν that satisfies the above inequalities so that we may state $2^\nu \geq 3\chi + 1 \geq 2^{\nu-1}$ and $2^\nu \geq 3\chi + 5 \geq 2^{\nu-1}$ if ν is even or odd, respectively, from which it follows that $2(3\chi + 5) \geq 2^\nu = N$. Hence, $2(3\chi + 5) \geq N \geq 3\chi + 1$. These results are shown in Fig. 8.

APPENDIX D: ADDITIONAL EXPERIMENTAL RESULTS

In the main text, we have presented results obtained on the IBM_BRISBANE QPU. In this appendix, to test the robustness of our conclusions, we provide results from additional IBM QPUs. These results, presented in Fig. 9, are in full qualitative agreement with our conclusions. Namely, in all cases, the CHaDD variants (rightmost column in the legend) outperform their underlying achromatic sequences (middle column in the legend).

[1] J. Preskill, Quantum computing in the NISQ era and beyond, Quantum **2**, 79 (2018).
[2] L. Viola and S. Lloyd, Dynamical suppression of decoherence in two-state quantum systems, Phys. Rev. A **58**, 2733 (1998).
[3] L. Viola, E. Knill, and S. Lloyd, Dynamical decoupling of open quantum systems, Phys. Rev. Lett. **82**, 2417 (1999).
[4] P. Zanardi, Symmetrizing evolutions, Phys. Lett. A **258**, 77 (1999).
[5] D. Vitali and P. Tombesi, Using parity kicks for decoherence control, Phys. Rev. A **59**, 4178 (1999).
[6] L. Viola and E. Knill, Random decoupling schemes for quantum dynamical control and error suppression, Phys. Rev. Lett. **94**, 060502 (2005).
[7] L. F. Santos and L. Viola, Enhanced convergence and robust performance of randomized dynamical decoupling, Phys. Rev. Lett. **97**, 150501 (2006).
[8] E. L. Hahn, Spin echoes, Phys. Rev. **80**, 580 (1950).
[9] H. Carr and E. Purcell, Effects of diffusion on free precession in nuclear magnetic resonance experiments, Phys. Rev. **94**, 630 (1954).
[10] S. Meiboom and D. Gill, Modified spin echo method for measuring nuclear relaxation times, Rev. Sci. Instrum. **29**, 688 (1958).
[11] A. A. Maudsley, Modified Carr-Purcell-Meiboom-Gill sequence for NMR Fourier imaging applications, Journal of Magnetic Resonance **69**, 488 (1986).
[12] D. Suter and G. A. Álvarez, Colloquium: Protecting quantum information against environmental noise, Rev. Mod. Phys. **88**, 041001 (2016).
[13] B. Pokharel, N. Anand, B. Fortman, and D. A. Lidar, Demonstration of fidelity improvement using dynamical decoupling with superconducting qubits, Phys. Rev. Lett. **121**, 220502 (2018).
[14] N. Ezzell, B. Pokharel, L. Tewala, G. Quiroz, and D. A. Lidar, Dynamical decoupling for superconducting qubits: A performance survey, Phys. Rev. Appl. **20**, 064027 (2023).
[15] G. Ravi, K. N. Smith, P. Gokhale, A. Mari, N. Earnest, A. Javadi-Abhari, and F. T. Chong, in *2022 IEEE International Symposium on High-Performance Computer Architecture (HPCA)* (IEEE, Seoul, South Korea, 2022), p. 288.
[16] C. Tong, H. Zhang, and B. Pokharel, Empirical learning of dynamical decoupling on quantum processors, PRX Quantum (2025).
[17] J. Jones and E. Knill, Efficient refocusing of one-spin and two-spin interactions for NMR quantum computation, J. Magn. Reson. **141**, 322 (1999).
[18] T. Tsunoda, G. Bhole, S. A. Jones, J. A. Jones, and P. J. Leek, Efficient Hamiltonian programming in qubit arrays with nearest-neighbor couplings, Phys. Rev. A **102**, 032405 (2020).
[19] V. Tripathi, H. Chen, M. Khezri, K.-W. Yip, E. Levenson-Falk, and D. A. Lidar, Suppression of crosstalk in superconducting qubits using dynamical decoupling, Phys. Rev. Appl. **18**, 024068 (2022).
[20] Z. Zhou, R. Sitler, Y. Oda, K. Schultz, and G. Quiroz, Quantum crosstalk robust quantum control, Phys. Rev. Lett. **131**, 210802 (2023).
[21] S. Niu, A. Todri-Sanial, and N. T. Bronn, Multi-qubit dynamical decoupling for enhanced crosstalk suppression, Quantum Sci. Technol. **9**, 045003 (2024).
[22] B. Evert, Z. G. Izquierdo, J. Sud, H.-Y. Hu, S. Grabbe, E. G. Rieffel, M. J. Reagor, and Z. Wang, Syncopated dynamical decoupling for suppressing crosstalk in quantum circuits, arXiv:2403.07836 [quant-ph].
[23] J. Bylander, S. Gustavsson, F. Yan, F. Yoshihara, K. Harrabi, G. Fitch, D. Cory, Y. Nakamura, J. Tsai, and W. Oliver, Noise spectroscopy through dynamical decoupling with a superconducting flux qubit, Nat. Phys. **7**, 565 (2011).
[24] G. A. Álvarez and D. Suter, Measuring the spectrum of colored noise by dynamical decoupling, Phys. Rev. Lett. **107**, 230501 (2011).
[25] G. A. Paz-Silva and L. Viola, General transfer-function approach to noise filtering in open-loop quantum control, Phys. Rev. Lett. **113**, 250501 (2014).
[26] L. M. Norris, G. A. Paz-Silva, and L. Viola, Qubit noise spectroscopy for non-Gaussian dephasing environments, Phys. Rev. Lett. **116**, 150503 (2016).
[27] V. Tripathi, H. Chen, E. Levenson-Falk, and D. A. Lidar, Modeling low- and high-frequency noise in transmon qubits with resource-efficient measurement, PRX Quantum **5**, 010320 (2024).
[28] J. A. Gross, É. Genois, D. M. Debroy, Y. Zhang, W. Mruczkiewicz, Z.-P. Cian, and Z. Jiang, Characterizing coherent errors using matrix-element amplification, npj Quantum Inf. **10**, 123 (2024).
[29] V. Tripathi, D. Kowsari, K. Saurav, H. Zhang, E. M. Levenson-Falk, and D. A. Lidar, Benchmarking quantum gates and circuits, Chem. Rev. (2025).
[30] P. Jurcevic *et al.*, Demonstration of quantum volume 64 on a superconducting quantum computing system, Quantum Sci. Technol. **6**, 025020 (2021).
[31] B. Pokharel and D. A. Lidar, Demonstration of algorithmic quantum speedup, Phys. Rev. Lett. **130**, 210602 (2023).
[32] B. Pokharel and D. A. Lidar, Better-than-classical Grover search via quantum error detection and suppression, npj Quantum Inf. **10**, 23 (2024).
[33] P. Singkanipa, V. Kasatkin, Z. Zhou, G. Quiroz, and D. A. Lidar, Demonstration of algorithmic quantum speedup for an Abelian hidden subgroup problem, arXiv:2401.07934 [quant-ph].
[34] E. Bäumer, V. Tripathi, D. S. Wang, P. Rall, E. H. Chen, S. Majumder, A. Seif, and Z. K. Minev, Efficient long-range entanglement using dynamic circuits, PRX Quantum **5**, 030339 (2024).
[35] E. Bäumer, V. Tripathi, A. Seif, D. Lidar, and D. S. Wang, Quantum Fourier transform using dynamic circuits, arXiv:2403.09514 [quant-ph].
[36] K. Khodjasteh and D. A. Lidar, Fault-tolerant quantum dynamical decoupling, Phys. Rev. Lett. **95**, 180501 (2005).
[37] K. Khodjasteh and D. A. Lidar, Performance of deterministic dynamical decoupling schemes: Concatenated and periodic pulse sequences, Phys. Rev. A **75**, 062310 (2007).
[38] G. S. Uhrig, Keeping a quantum bit alive by optimized π-pulse sequences, Phys. Rev. Lett. **98**, 100504 (2007).
[39] M. J. Biercuk, H. Uys, A. P. VanDevender, N. Shiga, W. M. Itano, and J. J. Bollinger, Optimized dynamical decoupling in a model quantum memory, Nature **458**, 996 (2009).
[40] G. S. Uhrig and D. A. Lidar, Rigorous bounds for optimal dynamical decoupling, Phys. Rev. A **82**, 012301 (2010).

[41] J. R. West, D. A. Lidar, B. H. Fong, and M. F. Gyure, High fidelity quantum gates via dynamical decoupling, Phys. Rev. Lett. **105**, 230503 (2010).
[42] Z.-Y. Wang and R.-B. Liu, Protection of quantum systems by nested dynamical decoupling, Phys. Rev. A **83**, 022306 (2011).
[43] J. R. West, B. H. Fong, and D. A. Lidar, Near-optimal dynamical decoupling of a qubit, Phys. Rev. Lett. **104**, 130501 (2010).
[44] Y. Xia, G. S. Uhrig, and D. A. Lidar, Rigorous performance bounds for quadratic and nested dynamical decoupling, Phys. Rev. A **84**, 062332 (2011).
[45] W.-J. Kuo, G. Quiroz, G. A. Paz-Silva, and D. A. Lidar, Universality proof and analysis of generalized nested Uhrig dynamical decoupling, J. Math. Phys. **53**, 122207 (2012).
[46] G. A. Álvarez, A. Ajoy, X. Peng, and D. Suter, Performance comparison of dynamical decoupling sequences for a qubit in a rapidly fluctuating spin bath, Phys. Rev. A **82**, 042306 (2010).
[47] G. Quiroz and D. A. Lidar, Optimized dynamical decoupling via genetic algorithms, Phys. Rev. A **88**, 052306 (2013).
[48] G. T. Genov, D. Schraft, N. V. Vitanov, and T. Halfmann, Arbitrarily accurate pulse sequences for robust dynamical decoupling, Phys. Rev. Lett. **118**, 133202 (2017).
[49] G. T. Genov, N. Aharon, F. Jelezko, and A. Retzker, Mixed dynamical decoupling, Quantum Sci. Technol. **4**, 035010 (2019).
[50] K. Khodjasteh and D. A. Lidar, Quantum computing in the presence of spontaneous emission by a combined dynamical decoupling and quantum-error-correction strategy, Phys. Rev. A **68**, 022322 (2003), erratum: *ibid*, Phys. Rev. A **72**, 029905 (2005).
[51] H. K. Ng, D. A. Lidar, and J. Preskill, Combining dynamical decoupling with fault-tolerant quantum computation, Phys. Rev. A **84**, 012305 (2011).
[52] G. A. Paz-Silva and D. A. Lidar, Optimally combining dynamical decoupling and quantum error correction, Sci. Rep. **3**, 1530 (2013).
[53] T. Unden, P. Balasubramanian, D. Louzon, Y. Vinkler, M. B. Plenio, M. Markham, D. Twitchen, A. Stacey, I. Lovchinsky, A. O. Sushkov, M. D. Lukin, A. Retzker, B. Naydenov, L. P. McGuinness, and F. Jelezko, Quantum metrology enhanced by repetitive quantum error correction, Phys. Rev. Lett. **116**, 230502 (2016).
[54] J. Conrad, Twirling and Hamiltonian engineering via dynamical decoupling for Gottesman-Kitaev-Preskill quantum computing, Phys. Rev. A **103**, 022404 (2021).
[55] A. Mena López and L.-A. Wu, Protectability of IBMQ qubits by dynamical decoupling technique, Symmetry **15**, 62 (2023).
[56] G. Quiroz, B. Pokharel, J. Boen, L. Tewala, V. Tripathi, D. Williams, L.-A. Wu, P. Titum, K. Schultz, and D. Lidar, Dynamically generated decoherence-free subspaces and subsystems on superconducting qubits, Rep. Prog. Phys. **87**, 097601 (2024).
[57] J.-X. Han, J. Zhang, G.-M. Xue, H. Yu, and G. Long, Protecting logical qubits with dynamical decoupling, arXiv:2402.05604.
[58] D. Leung, Simulation and reversal of n-qubit Hamiltonians using Hadamard matrices, J. Mod. Opt. **49**, 1199 (2002).
[59] M. Stollsteimer and G. Mahler, Suppression of arbitrary internal coupling in a quantum register, Phys. Rev. A **64**, 052301 (2001).
[60] M. Rotteler and P. Wocjan, Equivalence of decoupling schemes and orthogonal arrays, IEEE Trans. Inf. Theory **52**, 4171 (2006).
[61] P. Wocjan, Efficient decoupling schemes with bounded controls based on Eulerian orthogonal arrays, Phys. Rev. A **73**, 062317 (2006).
[62] M. Rötteler and P. Wocjan, in *Quantum Error Correction*, edited by D. A. Lidar and T. A. Brun (Cambridge University Press, Cambridge, 2013), Chap. 15, p. 376.
[63] A. D. Bookatz, M. Roetteler, and P. Wocjan, Improved bounded-strength decoupling schemes for local Hamiltonians, IEEE Trans. Inf. Theory **62**, 2881 (2016).
[64] D. Hayes, K. Khodjasteh, L. Viola, and M. J. Biercuk, Reducing sequencing complexity in dynamical quantum error suppression by Walsh modulation, Phys. Rev. A **84**, 062323 (2011).
[65] G. A. Paz-Silva, S.-W. Lee, T. J. Green, and L. Viola, Dynamical decoupling sequences for multi-qubit dephasing suppression and long-time quantum memory, New J. Phys. **18**, 073020 (2016).
[66] L. Shirizly, G. Misguich, and H. Landa, Dissipative dynamics of graph-state stabilizers with superconducting qubits, Phys. Rev. Lett. **132**, 010601 (2024).
[67] N. M. Linke, D. Maslov, M. Roetteler, S. Debnath, C. Figgatt, K. A. Landsman, K. Wright, and C. Monroe, Experimental comparison of two quantum computing architectures, Proc. Natl. Acad. Sci. **114**, 3305 (2017).
[68] K. Boothby, P. Bunyk, J. Raymond, and A. Roy, Next-generation topology of D-wave quantum processors, arXiv:2003.00133 [quant-ph].
[69] M. Sarovar, T. Proctor, K. Rudinger, K. Young, E. Nielsen, and R. Blume-Kohout, Detecting crosstalk errors in quantum information processors, Quantum **4**, 321 (2020).
[70] D. Bluvstein, H. Levine, G. Semeghini, T. T. Wang, S. Ebadi, M. Kalinowski, A. Keesling, N. Maskara, H. Pichler, M. Greiner, V. Vuletić, and M. D. Lukin, A quantum processor based on coherent transport of entangled atom arrays, Nature **604**, 451 (2022).
[71] R. L. Brooks, On colouring the nodes of a network, Math. Proc. Camb. Phil. Soc. **37**, 194 (1941).
[72] L. Lovász, Three short proofs in graph theory, J. Comb. Theory, Series B **19**, 269 (1975).
[73] R. Diestel, *Graph Theory* (Springer, Berlin, 2017), 5th ed.
[74] P. Wocjan and C. Elphick, New spectral bounds on the chromatic number encompassing all eigenvalues of the adjacency matrix, Electron. J. Combin. **20**, P39 (2013).
[75] T. Ando and M. Lin, Proof of a conjectured lower bound on the chromatic number of a graph, Linear Algebra Appl. **485**, 480 (2015).
[76] R. Karp, in *Complexity of Computer Computations*, The IBM Research Symposia Series, edited by R. E. Miller and J. W. Thatcher (Plenum, New York, 1972), Chap. 9, p. 85.
[77] Rigetti Computing, Rigetti systems, https://qcs.rigetti.com/qpus (2024).

[78] P. Nation, H. Paik, A. Cross, and Z. Nazario, The IBM Quantum heavy hex lattice, https://www.ibm.com/quantum/blog/heavy-hex-lattice (2021).
[79] A. Beutelspacher, Partial spreads in finite projective spaces and partial designs, Math Z **145**, 211 (1975).
[80] D. C. McKay, C. J. Wood, S. Sheldon, J. M. Chow, and J. M. Gambetta, Efficient Z gates for quantum computing, Phys. Rev. A **96**, 022330 (2017).
[81] A. Vezvaee, V. Tripathi, D. Kowsari, E. Levenson-Falk, and D. A. Lidar, Virtual Z gates and symmetric gate compilation, arXiv:2407.14782 [quant-ph].
[82] M. A. Nielsen, M. J. Bremner, J. L. Dodd, A. M. Childs, and C. M. Dawson, Universal simulation of Hamiltonian dynamics for quantum systems with finite-dimensional state spaces, Phys. Rev. A **66**, 022317 (2002).
[83] Y. Wang, Z. Hu, B. C. Sanders, and S. Kais, Qudits and high-dimensional quantum computing, Front. Phys. **8**, 589504 (2020).
[84] A. F. Brown and D. A. Lidar, Data Repository for "Efficient Chromatic-Number-Based Multi-Qubit Decoherence and Crosstalk Suppression," https://doi.org/10.5281/zenodo.15572005 (2025).